City Research Online

City, University of London Institutional Repository

This is the accepted version of the paper.

This version of the publication may differ from the final published version.

Permanent repository link: https://openaccess.city.ac.uk/id/eprint/21399/

Link to published version: http://dx.doi.org/10.1016/j.renene.2018.12.085

City Research Online: http://openaccess.city.ac.uk/   publications@city.ac.uk

Design and experimental evaluation of a parabolic-trough Concentrating Photovoltaic/Thermal (CPVT) system with high-efficiency cooling.

I.K. Karathanassis[a, b,1*], E. Papanicolaou[a], V. Belessiotis[a] and G.C. Bergeles[b,1]

[a] Solar & other Energy Systems Laboratory, Institute of Nuclear and Radiological Sciences & Technology, Energy and Safety, National Centre for Scientific Research DEMOKRITOS, Aghia Paraskevi, 15310 Athens, Greece

[b] Laboratory of Innovative Environmental Technologies, School of Mechanical Engineering, National Technical University of Athens, Zografos Campus, 15710 Athens, Greece

[*] Corresponding author:Ioannis.Karathanassis@city.ac.uk (I. K. Karathanassis).

[1] Present address: School of Mathematics, Computer Science & Engineering, City University London, Northampton Square, EC1V 0HB London, UK

Abstract. The design and performance evaluation of a novel parabolic-trough concentrating photovoltaic/thermal (CPVT) system are discussed in the present study. Initially, the system design and manufacturing procedures as well as the characteristics of the system sub-components are thoroughly illustrated. At a second stage, the findings in regard to the optical quality of the parabolic trough are presented, as obtained through an experimental procedure that utilizes a custom-made measuring device. The device bears a grid of sensors (photodiodes), so that the irradiation distribution on the receiver surface and the achieved concentration ratio can be determined. Besides, the main factors that have a significant effect on the trough optical quality were identified through ray-tracing simulations. The system electrical and thermal performance was subsequently evaluated in a test rig specially developed for that reason. Three variations of the system receiver incorporating different PV-module and heat-sink designs were evaluated and the prototype CPVT system was found to achieve an overall efficiency approximately equal to 50% (44% thermal and 6% electrical efficiencies, respectively) with a very weak dependency on the operating temperature.

Keywords: optical analysis, ray-tracing, experimental evaluation, parabolic trough, CPVT system

Nomenclature

CR	concentration ratio
C_p	specific heat, J/kgK
G	solar radiation flux, W/m^2
H	height, m
I	electric current, A
k	thermal conductivity, W/mK
L	length, m
$\dot{m}$	mass flow rate, kg/s
P_{el}	electrical power, W
Q_{th}	thermal power, W
S	length of distortion segment, m
T	temperature, K
U	uncertainty associated with a value
U_0	thermal losses coefficient, W/m^{2}K
t_s	solid substrate thickness, m
W	width, m
V	electric voltage, V

$\dot{V}_{tot}$		volumetric flow rate

Greek symbols

β		cell temperature coefficient, %/K
γ		receiver intercept factor
η_{el}		electrical efficiency
η_{th}		thermal efficiency
η_{tot}		total efficiency
η_0		optical efficiency
θ		incidence angle, $^{\circ}$
ρ		reflectance
τ		transmittance

Subscripts/Abbreviations

a		aperture, ambient
alpha		absorption coefficient
ave		average
b		beam
ch		channel
CR		concentration ratio
d		diffuse
el		electrical
EVA		ethylene-vinyl acetate
f		fluid
in		inlet
ins		insulation
max		maximum
min		minimum
out		outlet
PV		photovoltaic
MPP		maximum power point
ref		reference
refl		reflector
spec		specular
scat		scattered
th		thermal
tot		total
t		tape
w		wall

1. Introduction

The integration of an active cooling system into the receiver of a concentrating photovoltaic (CPV) system, apart from increasing the system electrical efficiency, makes the surplus heat available for utilization in other applications, where heat at temperatures in the range 60-80°C can be exploited, such as water and space heating, (adsorption or desiccant) cooling [1,2] or even desalination though membrane distillation [3,4]. The additional useful, thermal-power output leads to a significant increase of the system overall efficiency, while the reduced, in comparison to a flat-plate solar thermal collector, receiver dimensions render heat losses limited, an additional beneficial feature in terms of system overall efficiency.

Cooling is a major concern regarding the design of concentrating photovoltaics, as the integration of a heat dissipating configuration can have a beneficial impact on the system electrical efficiency. A wide variety of cooling configurations that could potentially be suited for the cooling of solar cells are presented in the review articles by Du et al. [5] and Royne et

al. **[6]**.   Besides, Micheli et al. **[7]** focused on the cooling options for concentrating photovoltaics that are made available through micro and nano-technology, such as micro-fins (or micro-channels) configurations, micro heat pipes and the use of carbon nanotube suspension as cooling fluid. Royne and Dey **[8]** proposed an active cooling system for densely packed cells comprising a grid of impinging jets. An optimization methodology, based on analytical models, was formulated in order to determine the layout and geometrical parameters of the cooling nozzles that maximize the cell electrical output. Barrau et al. **[9]** proposed a hybrid device that combines the techniques of impingement jets and microchannel-flow for cooling a dense array of solar cells under high concentration. Rahimi et al. **[10**] experimentally evaluated the performance of a water-cooled silicon cell module. Indoor testing using a solar simulator of 1000 W/m^2 showed that the cell power output increased by 30%.

The alternative technique of directly immersing a properly insulated PV module into the cooling fluid has also been examined. Han et al **[11]** conducted a comparative study in terms of optical transmittance and cooling capacity, in order to evaluate the applicability of different fluids for immersion cooling. Besides, Zhu et al. **[12]** experimentally investigated the cooling effectiveness of direct immersion of a solar cell module under concentrated sunlight (CR=160-200) into a liquid.

Few examples of integrated CPVT systems can be found in the open literature. Early studies by Chenlo and Cid **[13]** and Gibart **[14]** outlined the manufacturing procedure for prototype linear CPVT systems based on the Fresnel lens and the parabolic reflector technologies, respectively. Rectangular ducts were used to extract surplus heat in both studies. Coventry **[15]** designed and manufactured a parabolic trough linear CPVT system with a geometrical concentration ratio equal to 37. The receiver comprised an array of custom designed mono-crystalline silicon cells cooled by water flowing inside an aluminium tube. The system achieved thermal and electrical performance equal to 58% and 11%, respectively, for mass flow rates in the range 37.5-42.5 mL/s. Li et al. **[16]** evaluated the overall performance of a $2m^2$ prototype linear CPVT system, which used a parabolic reflector to concentrate solar radiation up to 31 suns. Three different types of cells (monocrystalline silicon, "super cells" and GaAs) were tested. The heat sink used for the cooling of the cell array was similar to that reported in **[15]**. The system employing the GaAs cell array obtained a maximum overall efficiency of 50.6%, with 41.7% and 8.9% attributed to the thermal and electrical efficiency, respectively.

Yongfeng et al. **[17]** performed a separate experimental evaluation for a variation of the system investigated in **[16]**, which achieves a concentration of 10x. The measured efficiency of the GaAs cells was 9.5% and the thermal efficiency of the system was 34%. Rossel et al. **[18]** manufactured a two-axis tracking 11x CPVT system. The system had an overall aperture area of 3.6 m^2 and employed Fresnel reflectors to concentrate irradiation onto a silicon cell module thermally bonded to a water cooled channel. The daily thermal efficiency of the system, without electricity production, was measured higher than 60%. Vivar et al. **[19]** report the performance evaluation of a Fresnel reflector linear system with concentration ratio 20x. A module of the system resembles a fully sealed case, which encloses two arrays of Fresnel reflectors that concentrate irradiation on two "micro-receivers" consisting of an array of silicon solar cells bonded to cylindrical tubes. Daily measurements established an average overall efficiency of 58% (50% thermal-8% electrical).

Chemisana et al. **[20]** proposed a design for a CPVT system that utilizes a linear Fresnel lens and a CPC (compound parabolic concentrator) as primary and secondary concentrators respectively. The system achieved a maximum concentration of 10x. A typical rectangular channel served as the cooling device with water flow inside it under laminar flow conditions. A 25x Fresnel lens linear CPVT system was integrated into a greenhouse as reported by

Sonneveld et al. [21]. Fresnel lenses were mounted onto the top glazing of the green house and concentrated the solar irradiation on tracking hollow beams, which were supported by the steel frame of the green house. Silicon solar cells were thermally bonded on the beams and water was circulated through them. Daily performance measurements showed an overall efficiency of 67% (56% thermal and 11% electrical). Nevertheless, the system optical losses (equal to 30%) were excluded from the calculation of the efficiency.

Chaabane et al. [22] manufactured a linear CPVT system that comprised an asymmetric compound parabolic reflector and a mono-crystalline silicon solar-cell module thermally bonded to a rectangular duct. The performance evaluation of the system showed that the maximum obtained thermal and electrical efficiencies were equal to 16% and 10%, respectively. Du et al. [23] evaluated the performance of an 8x linear Fresnel reflector system. At the system receiver, a silicon-cell module was bonded to a tube-on-plate heat sink with a U-shaped tube. Hourly measurements illustrated that the system thermal and electrical efficiencies under steady state conditions were approximately equal to 39% and 8% for coolant flow rates larger than 0.035 kg/s. Kribus et al. [24] proposed a miniature point-focus system with aperture area less than $1m^2$ that used a dish concentrator and high-efficiency, triple-junction cells operating at concentration of 500 suns. Nevertheless, although the system was reported to be under construction, experimental data of the system actual performance have not been published yet.

The evaluation of low-concentration, static CPVT systems has also been reported by a number of researchers. Kong et al. [25] manufactured a low concentration static linear CPVT system that employs a Fresnel lens and flat reflectors, as primary and secondary concentrators respectively, with a geometrical concentration ration of 5.7. For a single daily measurement, the system was reported to achieve peak electrical and thermal efficiencies equal to 10% and 56%, respectively. Brogren et al. [26] discussed the optical properties of the main components (reflector, glazing cells) comprising a 4x compound parabolic concentrator photovoltaic thermal system. The system optical efficiency was measured to be equal to 71%, while the system electrical and thermal output were measured equal to $330W/m^2$·cell area and $2300W/m^2$·cell area, respectively.

Nilsson et al. [27] focused on the annual performance of a static photovoltaic-thermal system employing asymmetrical parabolic concentrators. The annual electrical yield of the system was estimated at 373 kWh/m^2 cell area, while the thermal yield was 145 kWh/m^2 glazed area. Bernardo et al. [28] experimentally evaluated the performance of a low-concentrating parabolic CPVT system (CR=7.8). From a thermal performance point of view, the optical efficiency and the heat-loss coefficient of the system were measured equal to 45% and 1.9 W/K·m^2, respectively. The maximum electrical efficiency was 6.4%. Künnemeyer et al. [29] manufactured a static, low-concentration, V-trough CPVT module comprising four arrays of polycrystalline cells cooled by water flowing inside channels formed by the corrugated reflector frame. The overall efficiency of the system was in the order of 30%.

A novel linear Concentrating Photovoltaic Thermal (CPVT) system employing specially designed monocrystalline solar cells and microchannel cooling devices is evaluated in the present study. The main objectives of the study are to illustrate the design procedure and to highlight all the technical challenges associated with the development of a novel, linear-focus CPVT system and furthermore to experimentally evaluate the optical, electrical and thermal efficiencies achieved by the system. Furthermore, the present investigation constitutes a proof-of-concept study of the successful integration of two novel heat-sink configurations developed [30-33] in a prototype CPVT system. Three different system receiver configurations were considered employing different PV modules and cooling devices of different design layouts. In the subsequent sections, the technical specifications and geometrical parameters of the prototype system and its corresponding sub-components are

first presented, followed by the analysis of the system optical quality and the experimental evaluation of the system electrical and thermal efficiency.

2. Design and manufacturing of the prototype CPVT system

A rigid metallic structure that realizes the parabolic shape of the reflector and supports the receiver at the focal spot has been designed using three-dimensional CAD software (**Fig. 1a**) and manufactured (**Fig. 1b**). The structure comprises the frame, onto which the reflecting sheet and the receiver are seated, and the supporting arrangement, consisting of pillars and a circular base that is bolted to the ground. The reflector sheet is bolted on the parabolic profile of the frame, whereas the mounting of the receiver housing allows its translational displacement along the frame brackets, with its final position fixed using screw-nut assemblies. The parabolic profile is supported through metallic ribs mounted on the frame main axle. The supporting arrangement also comprises two axle joints, namely the joint between the main shaft and the supporting pillars and the rotating base discernable at the lower part of **Fig. 1a**. Hence, the frame can rotate around both the horizontal and vertical axes and thus two-axis tracking of the solar movement is possible. The parabolic frame realizes a concentrator with overall aperture area of 2.0 m^2 (active area of 1.0 m^2) and a focal length of 690 mm. The parabola width and height are equal to 2.0 m and 0.362 m, respectively, while its rim angle is equal to 71.9^o. Since the width of the parabolic frame is equal to 2.0m, the CPVT system active and overall aperture areas result equal to 1.0 and 2.0m^2, respectively, due to the fact that the active length of the PV module is equal to 0.5m, however the overall length of the receiver has been extended to 1.0m. This has been done, in order to mitigate end effects during the morning and afternoon hours, in the case that single-axis tracking was also considered and furthermore to accommodate the tubing and wiring required within the receiver. The frame was constructed of aluminum in order to make it lightweight and hence facilitate the collector tracking.
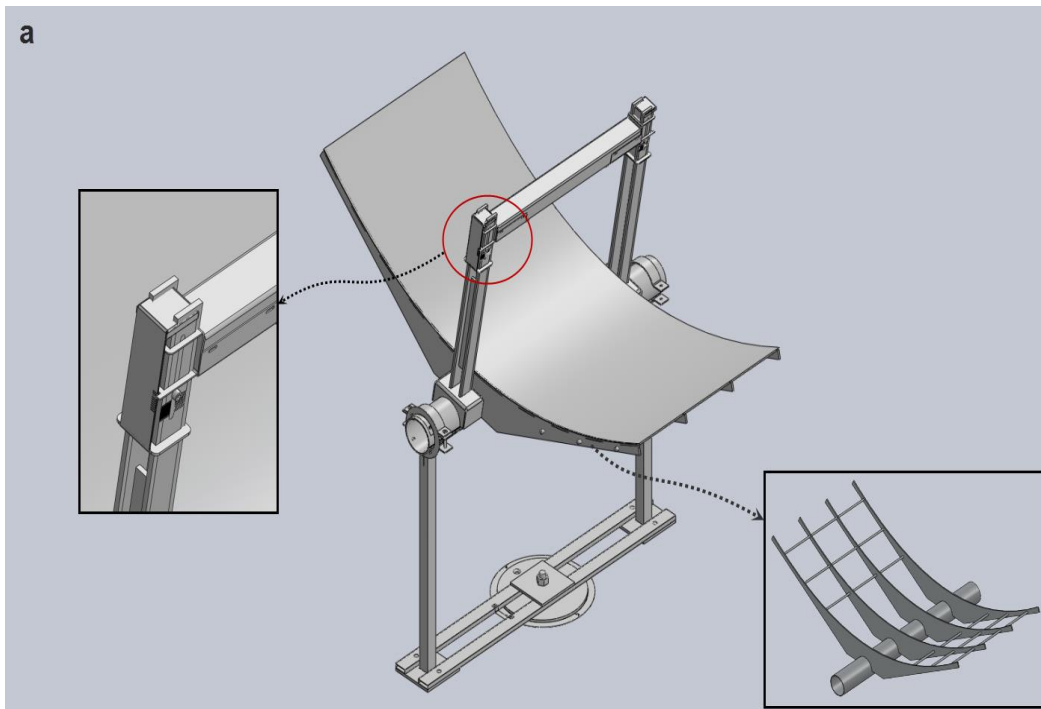
241

242   **Fig. 1** Metallic structure of the CPVT system: (a) CAD drawing and (b) constructed frame.

243

244   Commercially available anodized aluminum sheets (MIRO high-reflective 95) by *Alanod*
245   *Solar* were used as reflectors. The sheets specular reflectance is approximately equal to 92%
246   **[34]**. Custom solar cells were developed by *Narec Ltd*. The cells were manufactured by
247   monocrystalline silicon wafers of thickness equal to 150 μm and the most pronounced
248   difference in their design, compared to conventional cells, is the much higher finger density,
249   as depicted in **Fig. 2a**. In general mono-crystalline solar cells achieve higher efficiencies than
250   polycrystalline and thin-film cells **[35]**, while they have also been proven as more well suited
251   for concentrating applications of moderate concentration ratio (20<CR<100) **[15, 17, 28]** than
252   multi-junction III-V cells that require high concentration ratios (CR>200) **[36]**, in order to
253   perform efficiently.

254   Two cell designs were considered having widths of 40.0 mm ("narrow" cells) and 60.0mm
255   ("wide" cells), respectively. The 60.0mm width was dictated by the active width of the
256   employed cooling devices. The additional cell design having width of 40.0mm was
257   considered, in order to examine the effect of the extent of the mismatch between the cell and
258   solar band widths on the PV module electrical performance. The basic dimensions of the solar
259   cells are shown in **Fig**. **2b** and the most pronounced difference compared to a conventional
260   solar cell is the high finger density of the cell front electrical contact. The front contact was
261   optimized by Narec Ltd., which provided the cells, as a compromise between the capability of
262   the cells to handle increased current density due to the concentrated irradiation and the
263   reduction of their active area, since fingers, as metallic surfaces, are highly reflective. The
264   optimization methodology produced the finger arrangement that maximized the cell
265   efficiency. Ten cells were interconnected in series to fabricate a PV module, which comprises
266   a front cover made of low-iron glass, the PV laminate (EVA and solar cells) and a back
267   aluminum substrate. The cells were thermally bonded to the substrate using a thermally
268   conductive, yet electrically insulating, adhesive tape (k_t=0.6 W/mK).
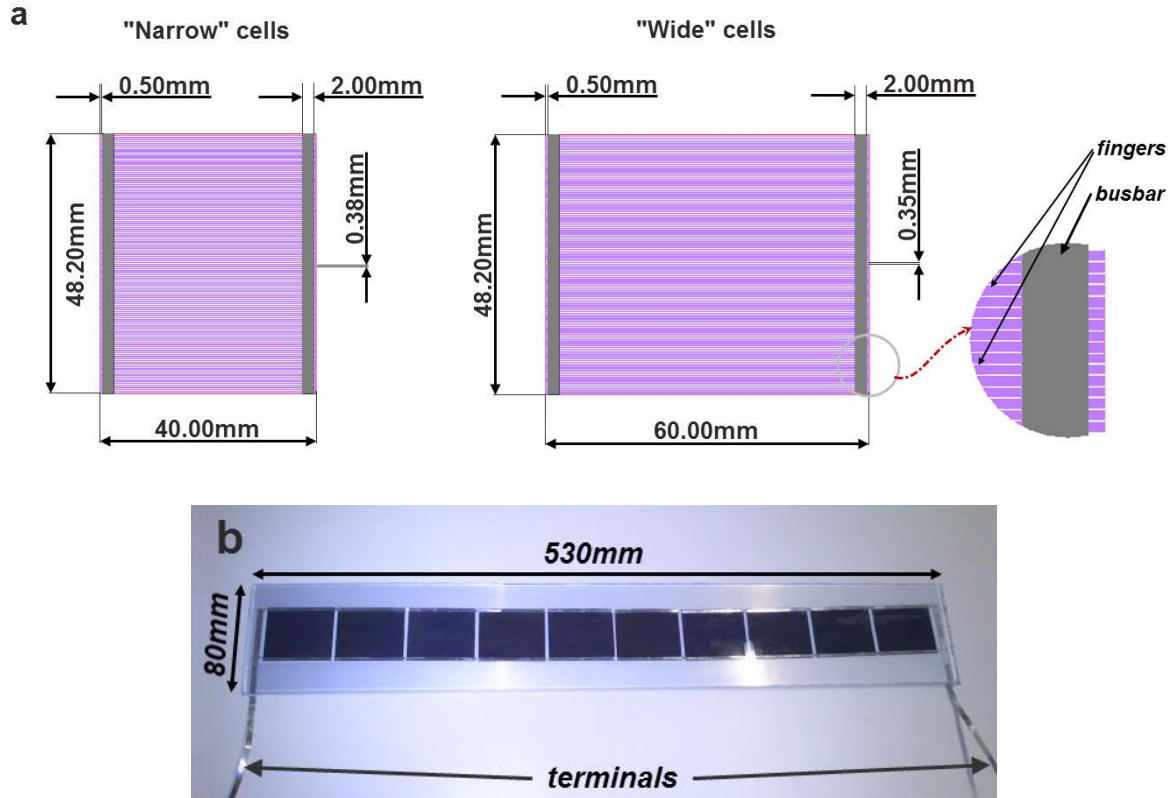
6

269

270
271
272 **Fig. 2** (a) Basic design parameters of the solar cells. (b) The assembled PV module.
273

274 Two plate-fin cooling devices of different layout have been integrated into the system.
275 More specifically the devices comprise two matching, elongated plate-fin heat sinks
276 employing microchannels of either constant (FW configuration) (**Fig. 3a**) or stepwise-varying
277 width (VW configuration) along three consecutive sections (**Fig. 3b**), respectively. From a
278 manufacturing/structural point of view the devices fulfill the general criteria of compact and
279 lightweight layout, reliable and leak-proof operation, viz. development of low internal
280 pressure, ease of fabrication using conventional machining and thus low cost and convenient
281 layout for thermal bonding to the solar cell module. The thermal and hydrodynamic
282 performance of the heat sinks has been thoroughly investigated by the authors in **[31-33]**,
283 while their geometrical parameters were determined using the optimization procedure
284 proposed in **[30]** by also taking into consideration the technical constraints posed by
285 conventional machining processes.
286 It has been verified through the previous studies **[31-33]** that the FW design (**Fig. 3a**)
287 obtains very low overall thermal-resistance values due to the large number of surfaces
288 (microchannels) available for heat transfer. The concept behind the design of the VW device
289 is to mitigate the pressure drop penalty, which is a major drawback of microchannel heat-
290 sinks, by employing two sections of low-fin density, as depicted in **Fig. 3b**. The complex
291 secondary flow pattern (longitudinal vortices) that emerges in the first two heat-sink sections
292 due to the effects of geometrical constrictions and buoyancy tends to disrupt the development
293 of the thermal boundary layer, hence increasing the thermal performance of the device despite
294 the subtraction of heat-transfer surfaces. In total, the VW device has been found to achieve a
295 superior hydrodynamic performance compared to the respective FW, with a minor decrease of
296 its thermal performance. Optimal devices in reference to each design have been manufactured
297 employing a multi-objective methodology, based on a genetic algorithm **[30]**.The total heat
298 sink length (500 mm) was dictated by the manufacturing procedure followed using a large-
299 scale milling machine. Likewise, the 65.0mm width was considered as the minimum ensuring

7

the rigidity of the device, since a very elongated and slender aluminum device would be prone to significant deformation during the soldering of the top heat sink cover.
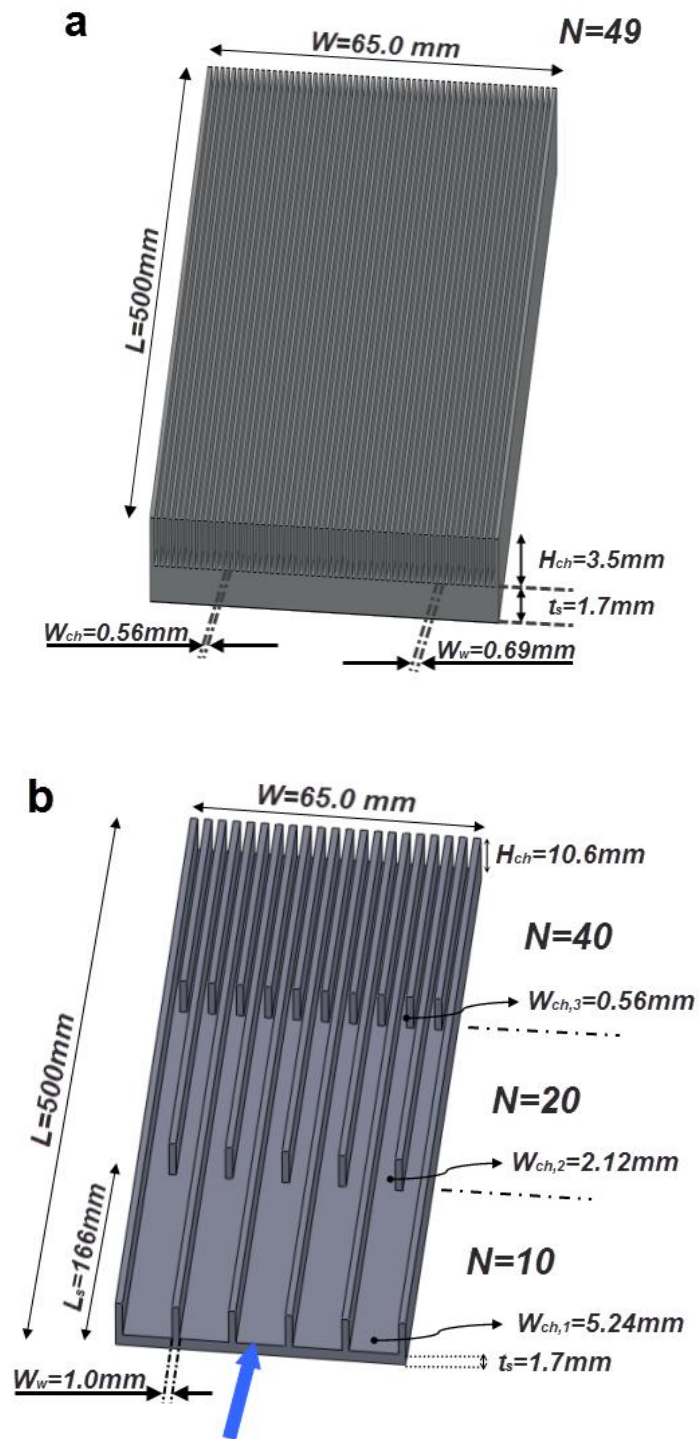

Fig. 3 Cooling devices employed in the CPVT system receiver: (a) FW configuration, (b) VW configuration.

3. Evaluation of the concentrator optical quality

3.1 Procedures followed for the experimental and numerical evaluation

An important first step in the present investigation is the measurement of the transversal and longitudinal irradiation flux distribution on the receiver. For this purpose, a measuring device was developed comprising an array of photodiodes properly mounted on the bottom surface of a rectangular hollow beam, as depicted in **Fig. 4**. The operation of the photodiode is in principal similar to that of a solar cell, in the sense that the current produced is proportional to the irradiation flux (e.g. in W/m^2) incident on the sensor aperture. The averaged flux incident on the sensor aperture is converted to signal and hence there is no influence of the irradiation incidence angle on its output. The so-called "cosine losses" [37], an intrinsic feature of non-perpendicular irradiation, corresponding to the radiation attenuation, as the incidence angle increases, has no effect on the accuracy of the flux measurement, since all the rays incident on the sensor aperture contribute to the overall power detected regardless of their angle of incidence. Besides, the suitability of photodiodes for measuring the intensity of concentrated solar irradiation has been demonstrated in a number of studies. Riffelmann et al. [38] and Lüpfert et al. [39] managed to measure the intercept factor and the optical losses of the EUROTROUGH solar-thermal collector prototype using a grid of photodiodes with diffuser filters mounted on a carriage that was positioned along the receiver length with the use of a linear actuator. Pihl and Thapper [40] measured the transversal irradiation distribution on the receiver of a low-concentrating CPVT system using a device comprising a photodiode mounted on a rotating base. Chong and Yew [41] illustrated the manufacturing procedure of a novel flux scanner employing photodiodes. An array of 25 photodiodes was mounted on a metallic frame that was able to move along two dimensions, thus producing a grid of measuring points.

The sensors are unable to detect the spatial non-uniformity of light irradiance within their active area; consequently a sensor of small size is required, especially when measuring the transversal distribution, which exhibits high variation within a short length. Photodiodes with rectangular aperture (5.4 x 4.3) mm^2 were used with tinted glasses as filters, in order to prevent overheating under concentrated sunlight. The tinted glasses also served as light attenuators to ensure that the photodiode response was well below the saturation region. Light collimators were placed on the tinted glasses to cut out the diffuse part of the irradiation so that the photodiode mainly detects the beam component of the light and also to prevent the filters from overheating and rupture. A highly reflective Mylar tape was adhered on the collimators in order to further reduce the heat absorbed by the filters. It was verified that the filters could remain up to three minutes under concentrated sunlight prior to their rupture, which is an adequate time interval to obtain meaningful results regarding the concentration. It must be noted that two variations of the measuring device were developed for measuring the longitudinal and transversal irradiation distributions, respectively. In regard to the longitudinal-measurement configuration, the distance between consecutive sensors was equal to 0.125 m and five photodiodes were placed to cover the entire receiver active length. Filters of circular aperture with diameter of 5.0 cm were placed over the photodiodes.

In order to measure the transversal irradiation-flux profile, five photodiodes were housed in holes drilled into an aluminum plate of dimensions 124 x 62 x 5 mm, which was subsequently mounted at the bottom face of the beam. The intermediate distance between sensors was equal to 15.0 mm, with the middle sensor being located exactly and the receiver mid-width. The plate was able to slide along the beam length allowing the measurement of the transversal profile at different longitudinal locations. A rectangular tinted glass was placed on

the plate to serve as filter, while the collimator had a narrow slit with width of 8 mm midway along its length.

The signal of the photodiodes was measured as current output, which is linearly proportional to the incident light power per unit area. The linear current response of the photodiode in proportion to the incident irradiation flux has been verified by the manufacturer and reported in the product datasheet [42]. The sensor linearity was further examined by retracting the light-attenuating filters from the grid of photodiodes and exposing them to direct sunlight. Excellent linearity of the sensors was verified with a correlation coefficient of 0.995. Additional calibration studies were conducted in order to verify that the sensor signal closely followed possible fluctuations of the solar irradiation intensity. The signals of all the sensors employed showed a very good general agreement with the maximum discrepancy detected in both the transversal and longitudinal-measurement configurations being approximately equal to 8% [43]. This value (8%) was used as the experimental uncertainty in the values of the concentration ratio presented and should be primarily attributed to misaligned mounting onto the supporting hollow beam. The concentration ratio CR values were calculated by dividing the output of the photodiodes under concentrated sunlight by the output of a photodiode placed at the upper surface of the device and therefore measuring the direct, one-sun irradiation, as shown in **Fig. 4**. Irradiation flux values were produced by all the detectors, which can handle both concentrated and parallel light, and thus the CR values could be readily estimated.
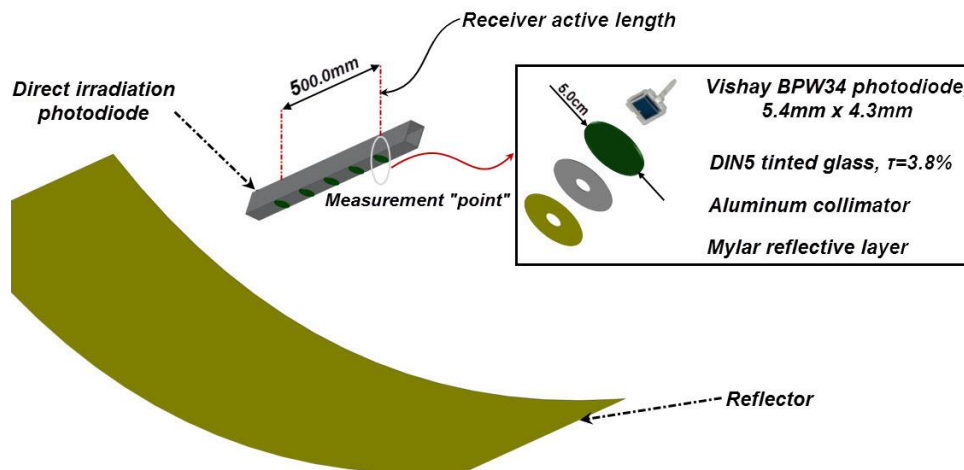

Fig. 4 Schematic of the device used for measuring the incident radiation on the system receiver.

In addition, a ray-tracing analysis was conducted in reference to the designed CPVT system, in order to predict the irradiation profile on the receiver. The analysis was performed with the commercial ray-tracing software TracePro [44], which utilizes the Monte Carlo method to predict the propagation of solar rays. A simplified geometrical model of the CPVT system was created, by omitting the supporting frame and base, and appropriate material properties were assigned to the system reflector and receiver, respectively. The solar irradiation was modeled as a circular sun source where all the radiation originates within a disc of radius 1.25m. The significantly larger sun-source area ($\approx$5m^2) compared to the CPVT overall area (2m^2) ensured a uniform irradiation flux density on the reflector aperture for a large number of rays. A proper power value was assigned to each ray, in order the overall radiation flux emitted by the source to be equal to the beam radiation measured (in the order of 1.0 kW/m^2) for each case investigated. The influence of the concentrator deformation on

the irradiation distribution on the receiver surface was considered to be much more significant compared to the effects of sun-shape and circumsolar radiation distribution, which exhibit significant variations depending on the geographical latitude and the time of the year.

The system receiver was modeled as a perfect absorber (*alpha=1.0*), as the focus is on the optical quality of the concentrator. In reference to the parabolic concentrator, two cases were considered, i.e. a perfectly specular mirror and an imperfect mirror that also induces light scattering (non-specular reflectance) due to surface and shape irregularities. In general, both specular and non-specular reflections occur simultaneously to some extent and the term "reflectance" is used for the ability of a material to reflect light in any manner **[45]**. Light scattering, i.e. widening of the solar band or beam spread has been taken into account in the ray-tracing simulations, in order to approximate the optical performance of the actual (imperfect) concentrator. The significance of light scattering induced by a surface was quantified in the simulations using the Bidirectional Scattering Distribution Function (BSDF), which is defined as the scatter radiance per unit incident irradiance:

$$BSDF = \frac{G_{scat}/\Omega}{G\cos\theta} \qquad (1)$$

where G_{scat} is the scattered irradiation within a solid angle Ω, and θ is the angle between the normal and a scattered ray. By imposing a value of the BSDF function, i.e. the "extent" of imperfections on the concentrator surface, a value of the specular reflectance is calculated by TracePro and the interaction of the incident rays with the imperfect concentrator is subsequently simulated. It becomes evident that the values of the concentrator specular reflectance explicitly corresponds to the extent of light scattering induced.

3.2 Irradiation-flux distribution on the receiver active surface

An initial step in regard to the ray-tracing simulations was to conduct numerical tests to confirm that the results produced are independent of the number of rays simulated. For this reason, two benchmark cases were selected for completeness purposes, one for high ($\rho_{spec}=\rho=0.95$) and the other for low ($\rho_{spec}=0.50$, $\rho_{tot}=0.95$) optical quality of the reflector, respectively. The number of simulated rays was gradually increased from $0.5 \cdot 10^6$ to $6 \cdot 10^6$, in order to illustrate the effect on the values of maximum and average concentration ratio *CR*, i.e. of the maximum and average irradiation flux on the receiver, as well as on the width of the solar band. The overall emitted irradiation flux was maintained equal to 1.0 kW/m^2 in all cases. **Table 1** summarizes the variation of the quantities in question for the two cases considered and increasing number of rays. As can be seen from the values of **Table 1**, the only quantity that exhibits some discrepancy with the number of rays is the maximum concentration ratio. The values of **Table 1** corresponding to both cases, in essence, illustrate that the irradiation distribution on the receiver is virtually identical regardless of the number of rays assigned, for a number of rays higher or equal to $2 \cdot 10^6$. It was finally decided to produce the results using $2 \cdot 10^6$ rays, which were found adequate for obtaining high accuracy and smooth irradiation profiles, within a reasonable simulation time of approximately four minutes on an eight-core CPU.

Table 1 Effect of the number of simulated rays on the produced irradiation profiles.

	$\rho_{spec}=0.95$			$\rho_{spec}=0.50$		
Rays($\cdot 10^6$)	**CR_{max}**	**CR_{ave}**	**W_{band} [mm]**	**CR_{max}**	**CR_{ave}**	**W_{band} [mm]**
0.5	113.4	22.5	62	62.2	14.2	123
1	112.6	22.5	62	61.8	14.3	123

| 2 | 112.5 | 22.5 | 62 | 61.7 | 14.3 | 123 |
| 4 | 112.4 | 22.5 | 62 | 61.7 | 14.3 | 123 |

Fig. 5 depicts the irradiation distribution on the receiver for concentrators of perfect parabolic shape and different optical quality with three values (0.95, 0.75, 0.50) being considered for the specular reflectance ρ_{spec}. It must be pointed out, that the material (overall) reflectance is equal to 95% in all the cases examined, however the specular reflectance ρ_{spec}, reduces according to the BSDF value (see **Eq. 1**) imposed, in order to replicate the effect of light scattering induced due to the reflector surface imperfections. The transversal profile shown in **Fig. 5a** exhibits a normal (Gaussian) distribution for fully specular reflection (ρ_{spec}=0.95). As the percentage of specular reflection decreases to 0.50, i.e. the concentrator optical quality decreases and significant light scattering occurs, on the one hand, the peak value of irradiation flux achieved decreases and, on the other hand, the form of the transversal distribution deviates from the Gaussian distribution. The solar band becomes wider and the profile exhibits plateaus of low concentration values at a distance spanning approximately between 20.0mm and 50.0mm from the receiver mid-with, as depicted on the magnified view of **Fig. 5a**. The form of the flux longitudinal profile, depicted in **Fig. 5b**, remains qualitatively unaltered regardless of the value of specular reflectivity. However, as can be clearly seen the concentration achieved at the focal line is approximately reduced by half as the specular reflectivity reduces from 0.95 to 0.50, in accordance to the peak value of the transversal profile. The receiver intercept factor was found to decrease in a linear manner with specular reflectivity meaning that a significant portion of the incoming sunlight on the collector aperture completely misses the receiver in the cases of non-specular reflectance and hence the CPVT system performance degrades.
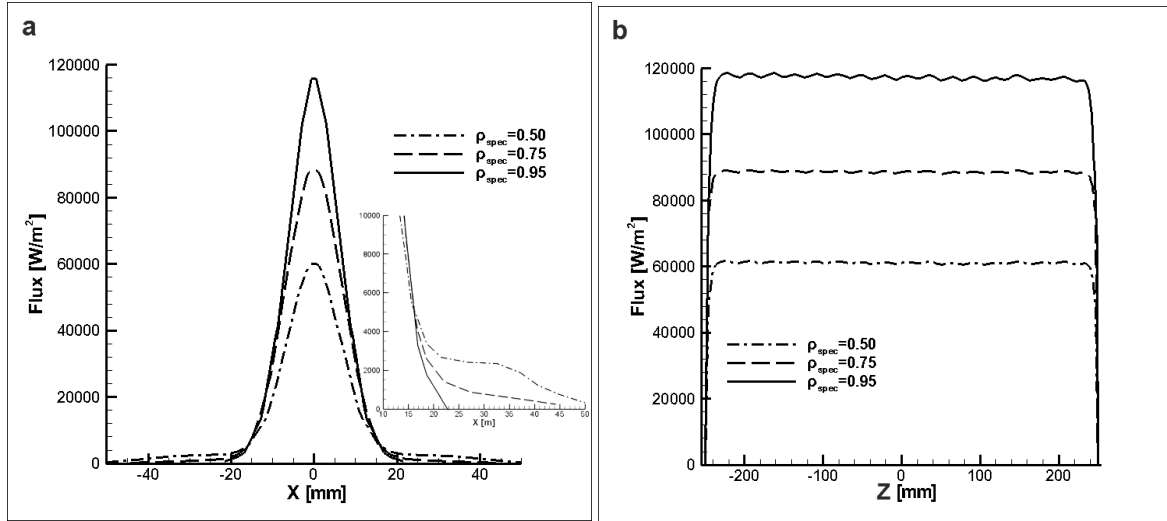

Fig. 5 (a) Transversal and (b) longitudinal profiles of the irradiation distribution for concentrators of perfect parabolic shape and different optical quality.

It was made clear from **Fig. 5a** that the transversal irradiation distribution exhibits a clearly discernible peak at the receiver mid-width, regardless of the optical quality of the concentrator. However, the irradiation measurements revealed a different transversal profile with two regions of high irradiation intensity located on either side of the receiver centerline, while the irradiation at the location where maximum irradiation was expected (receiver mid-width), actually exhibited low concentration values. The fact that the profile exhibited (relative) symmetry allowed the conclusion that the characteristic, dual-peak distribution did not occur due to tracking error. Furthermore, since a two-axes tracking system was employed

during the investigation, the solar irradiation was always perpendicular to the CPVT system aperture and thus there were no optical mechanisms (e.g. cosine or end losses) that could have possibly affected the form of the irradiation distribution on the receiver, which should have a typical Gaussian distribution. Therefore, the "dual-peak" profile must be attributed to the shape quality of the concentrator. An angular deviation of the parabola from its ideal shape, would in essence indicate that the actual focal length is different than the ideal one, e.g. see [45]. However, it has been demonstrated that off-focus operation tends to widen the focal band and produce a smoother irradiation profile. It was postulated that the shape of the parabola was distorted in the sense that the parabola apex was not a single point but instead a flat segment, denoted as *S* in **Fig. 6**, resulting in the existence of two focal points. This assumption can be supported by the procedure followed for the construction of the parabolic frame, as the metallic ribs that realize the parabolic shape were manufactured as two separate, symmetrical parts that were subsequently welded on the frame main shaft. The thickness of the welding joints, which are visible at the inset of **Fig. 6**, is small yet inevitably displaces the symmetrical ribs and distorts the shape of the parabola. Ray-tracing simulations were conducted to illustrate the effect of the distorted parabolic shape on the irradiation profile on the receiver. As was already mentioned, the displacement of the ribs must be small and thus values between 10.0 mm and 40.0 mm were considered as length for the segment *S*.
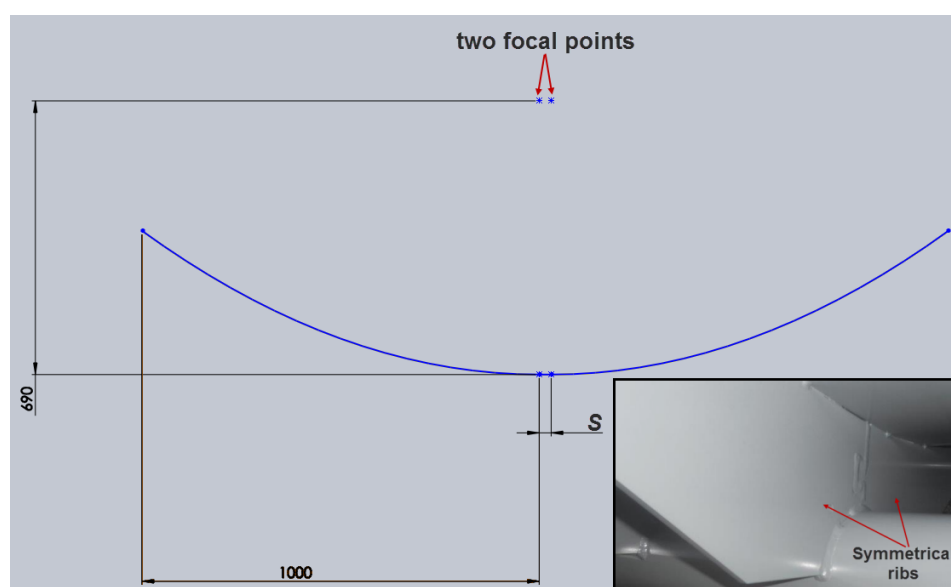

Fig. 6 Distorted form of the reflector parabola due to manufacturing imperfections.

Fig. 7a presents the solar irradiation bands incident on the receiver for incremental geometric distortions of the parabolic concentrators, as produced by the simulations. It can be observed that two illuminated regions on either side of a dark region appear for values of the flat segment length S equal to or larger than 20mm. As the distortion length increases the two peaks shift away from the receiver center-line and the middle dark area becomes wider. In addition, the maximum irradiation intensity is significantly decreased for S=20.0 compared to that for S=10.0 mm. It is therefore made evident that small errors in the shape of the parabola can have a remarkable effect on the reflected radiation distribution. An actual photograph of the receiver under concentrated illumination is presented in **Fig. 7b** for comparison, where it can be clearly discerned that the center part of the cells remains un-illuminated, while two lines of high concentration are evident on either side of it. A thermal image of the receiver in operation, depicted in **Fig. 7c,** also demonstrates that the central part of the PV module

remains cool, while two linear regions, corresponding to the illuminated regions evident in **Fig. 7b**, of high temperature are evident on both sides of the central region. It can be therefore concluded that the actual irradiation distribution is accurately represented by the ray-tracing simulations.
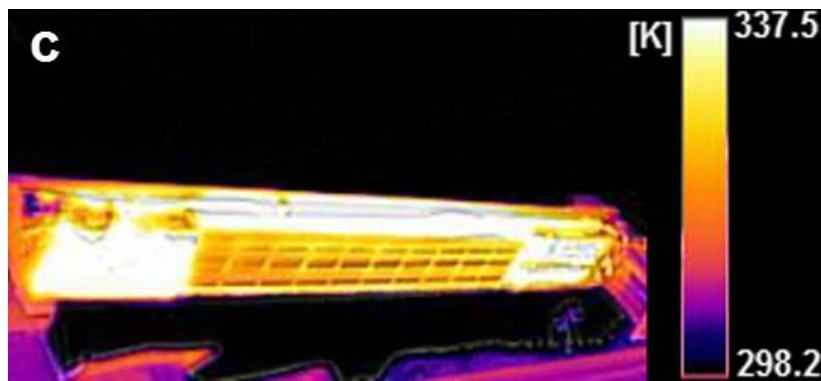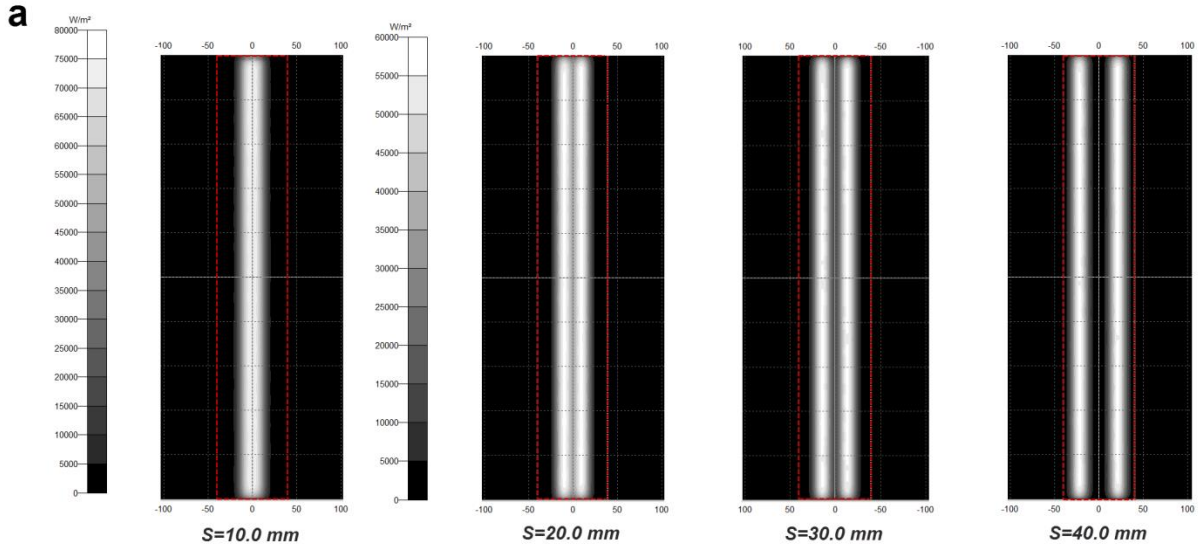

Fig. 7 (a) Solar irradiation bands incident on the receiver for different lengths of the *S* segment (ρ_{spec}=0.95). (b) Actual illumination pattern on the receiver of the CPVT system. (c) Thermal image of the system receiver.

The "twin-peak" profiles are clearly evident in **Fig. 8** for S ≥20.0mm. Despite the profile maintaining a single peak for S=10.0, the maximum concentration is reduced compared to a perfect parabola. An additional observation, which applies for all two-peak cases regardless of the value of specular reflectivity, is that the maximum flux value obtained remains constant and unaffected by the length of the segment S. By comparing **Fig. 8** to **Fig. 6a**, it is made clear that the maximum concentration achieved by a pseudo-parabolic shape having two focal points is approximately half of that achieved by a geometrically perfect parabola. It must also be mentioned that the profiles for each value of S exhibit a similar qualitative form for the three values of specular reflectance considered.

Special attention must be given to **Fig. 8c**, where the concentration values measured across the receiver width at five locations along the receiver active length (Z=0.125, 0.250, 0.375 m) are also presented. It must be pointed out that the ray-tracing results presented correspond to $\rho_{spec}=0.50$, indicating that the concentrator induces significant scattering of the reflected radiation. As can be seen, the experimental points do lie between the predicted profiles for S=30.0 mm and S=40.0 mm, but they clearly follow the same trend, i.e., with alternating regions of low and high concentration. The asymmetry that can be discerned at the points with X=±15.0 mm could be due to displacement of the rib, as it could not be guaranteed that the parabolic frame is perfectly symmetrical. Besides, the measurements at the three longitudinal positions do not coincide, indicating that the parabolic frame is imperfect in a three-dimensional sense.

The error in the receiver vertical displacement relative to the exact focal line can also have a considerable effect on the flux distribution. The profile depicted with a red line in **Fig. 8c** corresponds to a displacement error of 0.73% (f ′=685.0 mm) in the receiver position and a concentrator with distortion S=30.0 mm. It is evident that the profile is noticeably different from the respective case with no displacement error. The profile is in fair agreement with the experimental measurements and it is regarded as the best approximation of the flux profile on the receiver. It is important to point out that the actual deformation of the concentrator is anisotropic in a manner that cannot be predicted. An averaged effect of the surface imperfections was imposed for the ray-tracing simulations through the BSDF values, along with a characteristic deformation attributed to the lateral displacement *S*. However, the full three-dimensional topology of the trough deformation cannot be captured by the simulations nor the "point" solar-flux measurements. The distinct pattern of regions having low and high illumination, clearly discernible in **Figs. 7b-c**, is clearly captured by the measurements, as also by the simulations. Furthermore, the numerical and experimental evaluation allowed the estimation of the maximum irradiation flux on the receiver surface, which was demonstrated to be in the order of 25000-30000 W/m^2.
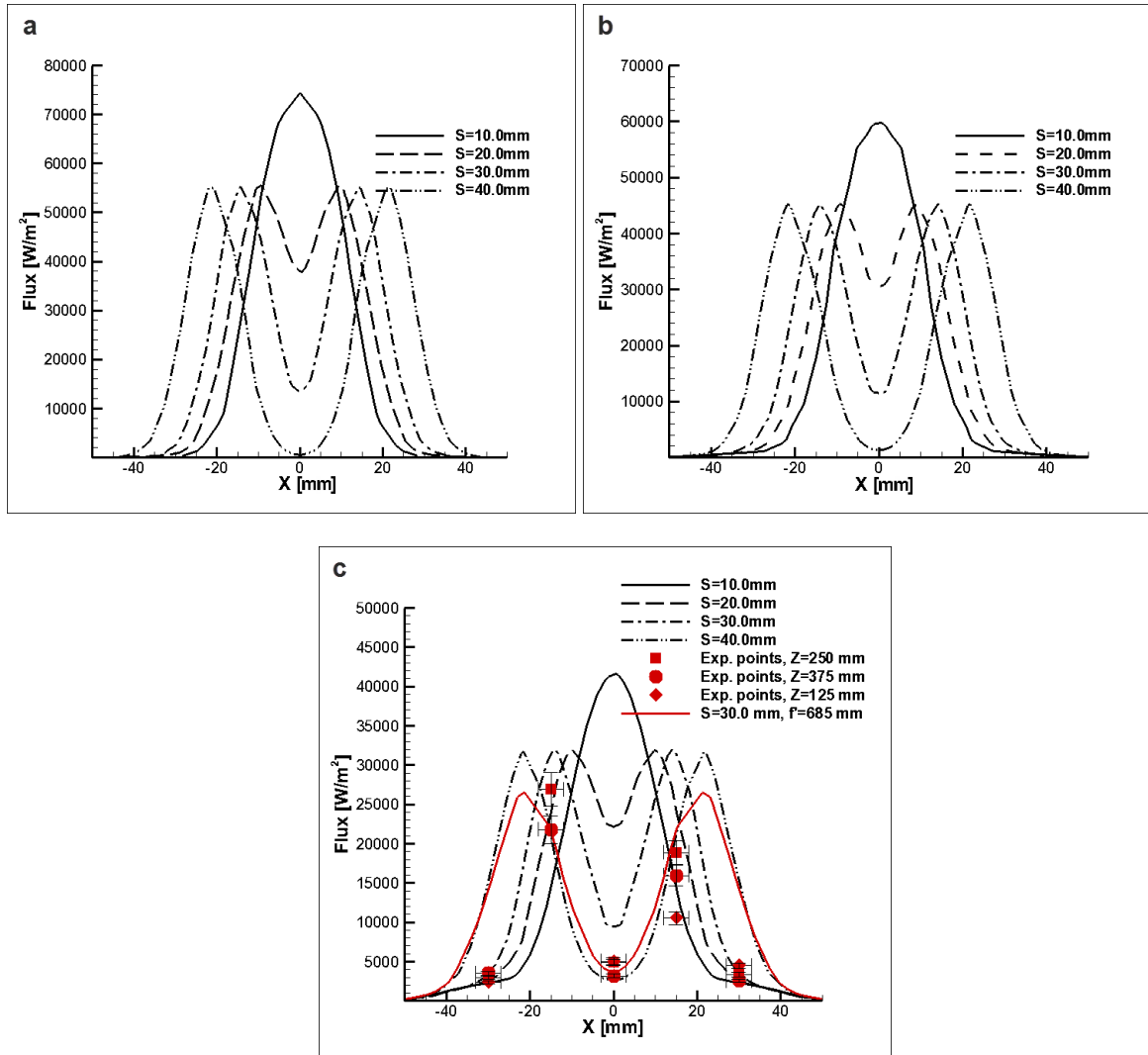
Fig. 8 Transversal profiles of the irradiation distribution for "distorted" concentrators of different optical quality: (a) ρ_{spec}=95%, (b) ρ_{spec}=75%, (c) ρ_{spec}=50%.

Fig. 9 presents the longitudinal flux profiles for concentrators of different quality and distortion. The length of the segment S has no effect on the qualitative form of the longitudinal profiles but only affects the flux intensity. The profiles for S≥20.0 mm correspond to the transversal locations on the receiver, where peak concentration is obtained. The experimental values of the flux intensity measured along the receiver active length are also included in **Fig. 9b**. The length-wise distribution of the flux intensity clearly reveals that the parabolic frame is imperfect in a three-dimensional sense, as the concentration varies along the receiver length as well. The experimental values regarding the first peak are in good agreement with the ray-tracing prediction for ρ_{spec}=0.50, S=30.0 mm and f'=685 mm, which, as was also mentioned for the transversal profile, appears to be the most reliable approximation of the actual distribution. On the other hand, the measured flux values corresponding to the second peak are lower than the predicted ones. This discrepancy, which is also evident in **Fig. 8c**, could be attributed to an increased slope error associated with only the one of the two symmetrical ribs that tends to widen the specific solar band. The slope error could be a result of imprecise manufacturing of the specific rib, but it is far more plausible to assume that the error occurs due to the uneven thickness of the punch-welding joints that bond the aluminum sheet realizing the parabola onto the ribs. As the welding joints are distributed along all the ribs and, in addition, there are several joints along the length of

16

584 each rib, they can be identified with great certainty as the main cause of the three-dimensional
585 distortion of the parabolic surface, which consequently leads to a fully three-dimensional
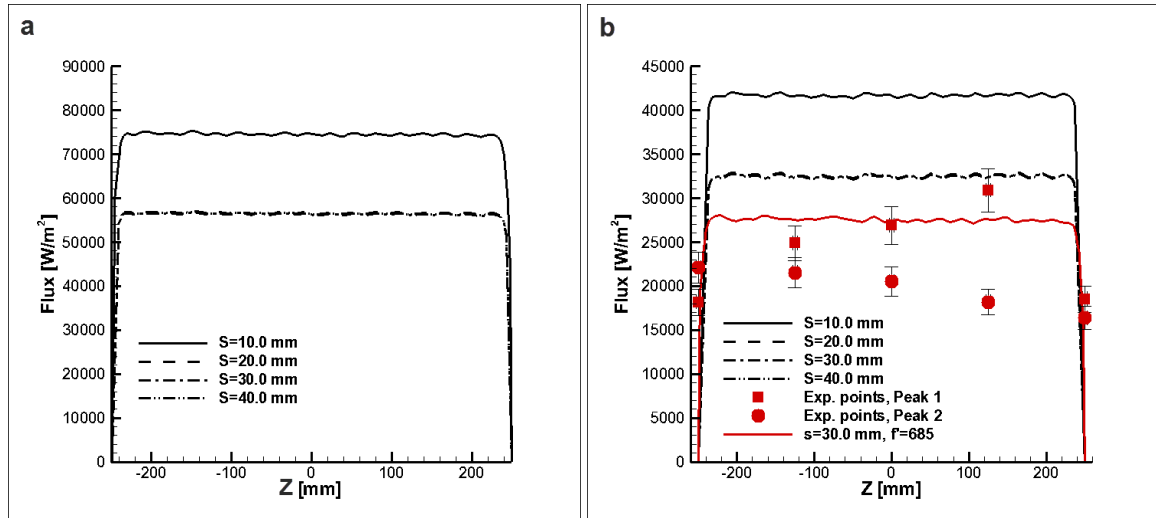586 pattern of the scattered solar rays on the receiver surface.
587

590 **Fig. 9** Longitudinal profiles of the irradiation distribution for "distorted" concentrators of different optical
591 quality: (a) ρ_{spec}=95%, (b) ρ_{spec}=50%.

4. Experimental evaluation of the CPVT system overall performance

4.1 Description of the experimental setup

597   The electrical and thermal performance of the CPVT system was evaluated in an outdoor
598 testing rig specially developed for this purpose (**Fig. 10**). The experimental setup comprised
599 the electrical and hydraulic circuits, as well as the necessary instrumentation for the
600 measurement of the quantities needed for the characterization of the system overall
601 performance. It is important to point out that the prototype system does not include a storage
602 tank and therefore there is no additional device intervening in the delivery of the thermal
603 power produced to the thermal load. As illustrated by Fig. 10, the produced thermal power is
604 eventually dissipated to the environment through the cooling unit (CU) incorporated in the
605 test rig, which acts as the thermal load for the purposes of the performance evaluation.
606   Direct radiation G_b was calculated by subtracting the diffuse radiation G_d from the total
607 radiation G_{tot}. For this purpose, two properly calibrated *Kipp & Zonen* (SMP 11)
608 pyranometers of secondary-standard accuracy [46] were used. One instrument was mounted
609 on the collector frame and tracked the movement of the sun in order to measure the total
610 radiation perpendicularly incident on the collector, while the second was mounted on a static
611 pillar beside the collector and was properly shaded using an appropriate ring manufactured by
612 *Kipp & Zonen*, so as to detect only the diffuse part of the solar radiation. A properly shaded
613 four-wire Pt100 temperature sensor manufactured by *Thies Klima* was used for the
614 measurement of ambient temperature. A cup anemometer manufactured by *Thies Klima* was
615 used for the measurement of the wind velocity. Water flow rate in the hydraulic circuit was
616 measured with a ring piston flow meter manufactured by Aqua Metro. Two four-wire Pt100
617 temperature sensors were used for the measurement of the fluid temperature at the inlet and
618 the outlet of the collector. The temperature at the solid substrate of the PV modules and the
619 heat sinks was measured with the use of type T (copper-constantan) thermocouples
620 manufactured by *OMEGA*. A variable resistor (0-6Ω) capable of dissipating up to 200W to

17

the environment was used as electric load, in order to operate the solar-cell module at the point of maximum power production. The voltage across the module was directly measured by the data logger through additional copper wires soldered to the module leads, so as to avoid any voltage drop in the high current cables. The produced current was converted to voltage through a 1 mΩ shunt resistor and consequently measured by the data logger. The use of an analogue, variable-resistive load was deemed as a reliable and inexpensive solution to measure the I-V curves of the solar-cell modules. The power output of the PV modules for each value of the load, was directly measured by the data logger and thus it is not associated with any error. The operating point of maximum power output was also stored by the data logger. The signals of all instruments were carried to an Agilent 34901A data logger and the measured values were processed and stored to a computer using the Agilent VEE software [47]. Data were logged and stored in a file every five seconds.
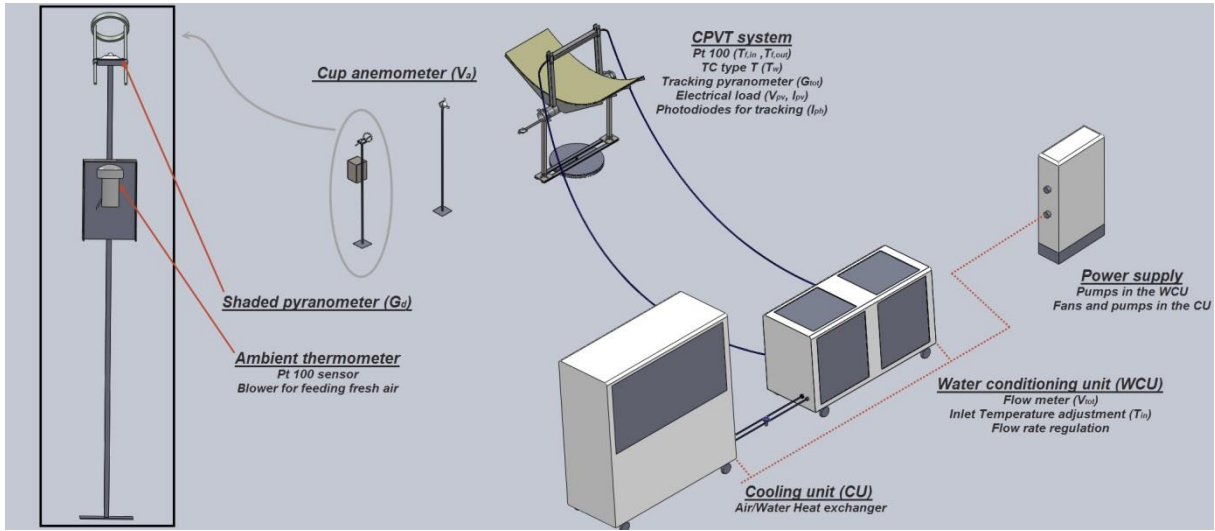

Fig. 10 Layout of the test rig developed for the evaluation of the system.

4.2 Experimental uncertainty analysis and propagation of errors

An uncertainty analysis based on propagation of errors, as described in [48], has been conducted in order to determine the resulting uncertainty of the calculated quantities due to the error associated with the direct measurement of primary quantities. Considering that a result R is calculated from a set of measured quantities x_i, $R = R(x_1, x_2, x_3,...,x_i)$; then the uncertainty in the calculated value is equal to:

$$U_R = \left[\sum_{i=1}^{N} \left(\left(\frac{\partial R}{\partial x_i} \right) U x_i \right)^2 \right]^{\frac{1}{2}}$$

(2)

where $U x_i$ is the uncertainty associated with the measurement of the values x_i. **Eq. (2)** is valid regardless of whether the measurement uncertainty is given in absolute or relative values. The uncertainty in the values of the measured quantities required for the system characterization are given for a confidence level equal to 95% and summarized in **Table 2**. In addition, it must be pointed out that the error in the electrical signals directly measured by the data logger was considered negligible, while the uncertainty in the measurements of the solar radiation, the volumetric flow rate and the fluid temperature presented in **Table 2** have been determined by

calibration procedures performed in the Solar and other Energy Systems Laboratory. The uncertainty associated with quantities deriving from the directly measured ones was calculated by making use of **Eq. (2)** and are presented in **Table 3**.

Table 2 Uncertainty in measured quantities.

Measured quantity	Uncertainty U
V_{air} [m/s]	1.90%
T_a [K]	0.054
G_{tot} [W/m^2]	1.41%
G_d [W/m^2]	1.41%
$\dot{V}_{tot}$ [m^3/s]	1.76%
T_f [K]	0.054 K
T_w [K]	0.5 K
V_{pv} [V]	-
I_{pv} [A]	-
W [m]	0.025%
L [m]	0.1%

Table 3 Uncertainty in calculated quantities.

Calculated quantity	Uncertainty U
A_a [m^2]	0.10%
G_b [W/m^2]	1.99%
Q_{th} [W]	2.29%-2.90%-3.46%
P_{el} [W]	-
η_{th} [-]	3.52%
η_{el} [-]	2.05%
η_{tot} [-]	4.06

4.3 Environmental and operating conditions

The performance of the integrated CPVT system was assessed for three variations of the system receiver comprising different PV module-heat sink combinations aiming at clearly illustrating the influence of the performance characteristics of receiver constituents on the overall efficiency and possibly designate the most attractive configuration. The efficiency measurements presented in the following paragraphs were performed in the summer and autumn period of 2014 at a latitude of 38°. The direct beam radiation, wind velocity and ambient temperature varied within the ranges 760-970 W/m^2, 0-2 m/s and 288-308K respectively, for all the testing sequences. Two-axes tracking of the solar irradiation was realized in all test cases, in order to avoid the effect of cosine and end losses on the performance of the CPVT system. Perpendicular irradiation was verified through the maximization of the output signal of a photodiode placed at the upper surface of the system receiver.

4.4 Characterization of the PV-modules electrical performance

681   An initial stage for the assessment of the modules electrical performance was to determine
682 the IV curves that characterize their operation under concentrated sunlight. For a specified
683 flow rate of the cooling fluid, the system was allowed to reach steady-state conditions and
684 then the value of the external load was gradually varied between its minimum and maximum
685 values (0-6 Ω), so as to cover the entire operating range of the modules. Measurements were
686 taken every 5 s and enough experimental points were obtained within two minutes, in order to
687 derive the I-V curve. Hence, the I-V curve for each module could be obtained for, in essence,
688 a constant irradiation value, constituting the measurement reliable. **Fig. 11** presents the
689 experimental points obtained for two PV modules assembled with narrow (**Fig. 11a**) and wide
690 (**Fig. 11b**) cells, respectively. The IV curves for one-sun irradiation as resulted from a flash-
691 tester measurement (at $T_{ref} = 25^{o}C$) are also included in the figures for comparison. It can be
692 discerned that the modules regardless of the cell design obtained an open circuit voltage V_{OC}
693 approximately equal to 6.2V. However, the module with the wide (60.0mm) cells produced a
694 short circuit current I_{SC} approximately equal to 12A, considerably higher compared to the
695 approximately 9A produced by the module comprising narrow (40.0mm) cells. It is essential
696 to point out that the solar-cell modules under concentrated irradiation has a power output in
697 the order of 55-75W, while the power output for typical solar irradiation is in the order of 3W.
698 The enhanced electrical output of the wide-cell module should be primarily attributed to its
699 larger active area, since the solar band has been significantly widened due to excessive light
700 scattering induced by the concentrator surface imperfections, as was demonstrated in the
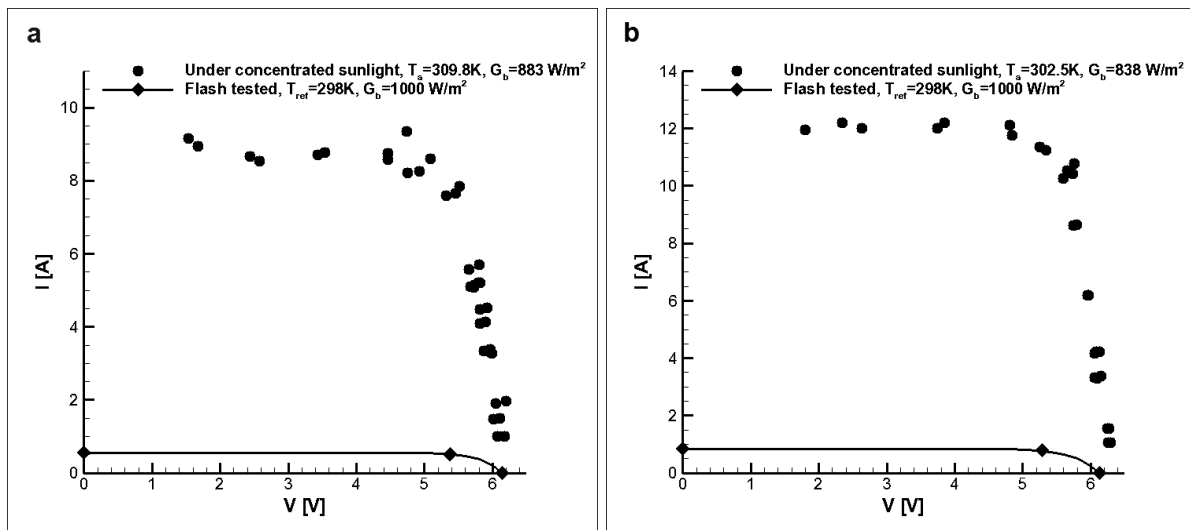701 previous paragraph.
702

705 **Fig. 11** IV Curves for (a) the narrow-cell module and (b) the wide-cell module.

707   The solar-cell modules were operated under concentrated sunlight without the presence
708 of a heat sink, in order to evaluate the deterioration in their performance due to the elevated
709 temperature. The resistive load was appropriately fixed so that the modules operated close to
710 their maximum power point. The produced electrical power, the module temperature along
711 with the direct solar irradiation and the ambient temperature were recorded at intervals of 3s,
712 in order to keep the overall time period of each testing sequence as short as possible and thus
713 minimize any effect on the results of a possible fluctuation of the environmental conditions or
714 temporary loss of normal incidence. Two type-T thermocouples symmetrically attached to the
715 mid-width of the back substrate were used for the measurement of the module temperature.
716   **Fig. 12** shows the relative change in the module performance as a function of the
717 temperature difference to ambient. The results were taken on consecutive clear days under

slightly different environmental conditions and good repeatability of the measurements was achieved. As made evident by both **Figs. 12a and 12b**, the expected linear decrease in performance is verified **[49]**. However, the rate of decrease is steeper in the case of the "narrow" solar cells, which is a clear indication that the "wide" cells are better suited for operation at elevated temperature. The difference in the behavior of the two cell designs can be attributed to the series-resistance value that characterizes each design. According to the values provided by the manufacturer, the series-resistance value is higher for the narrow-cell module, equal to 0.70 Ω instead of 0.49 Ω for the wide-cell module, and by taking in mind that the series-resistance increases linearly with temperature **[50]**, the power dissipation within the module and thus the performance deterioration is more pronounced for the narrow cells.
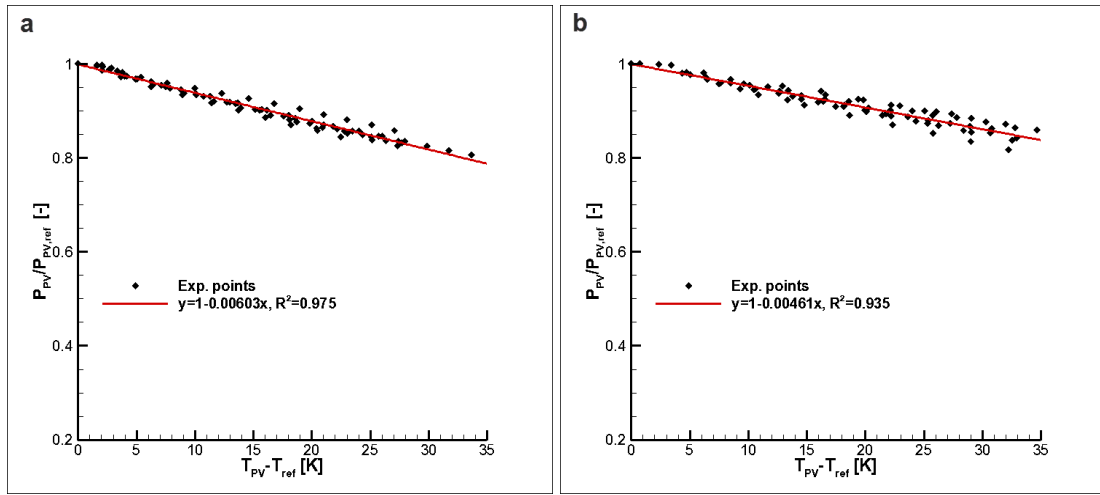

Fig. 12 Effect of temperature on the solar-cell module performance: (a) narrow cells, (b) wide cells.

4.5 Thermal and electrical performance of the CPVT system

At the present time, there is no official standard available for the performance characterization of CPVT systems **[51]**. Therefore, and regarding the system thermal performance in particular, the quasi steady-state method **[52,53]**, which applies to concentrating solar thermal collectors, was employed. According to the method, the system efficiency is determined for a set of prescribed operating conditions, while requirements are also posed for the prevailing environmental conditions. The limits regarding the prevailing environmental conditions, as well as the constraints posed on the variation of the main physical quantities, in order for the experimental test to be considered valid are shown in **Table 4**.

The flow rate selected for the measurement of the system thermal efficiency should represent actual operating conditions, while the PV module should be operated at the maximum power point. The time interval required for obtaining an experimental point must be in the order of 3-5 minutes and thus the rotating base of the CPVT system allows the acquisition of a large number of experimental points in each testing sequence, as near-normal incidence can be achieved throughout the entire daylight period, reducing in this way the evaluation time period.

Table 4 Requirements of the quasi steady-state method.

Absolute constrictions	
V_{air}	<4.5 m/s

G_b	$>630\ \text{W/m}^2$
$G_{b,max}$-$G_{b,min}$	$>200\ \text{W/m}^2$
θ	$\approx 0^\circ$

Constraintss in variance	
T_{in}	1% or 0.2°C
$T_{f,out}$-$T_{f,in}$	4% or 0.4°C
$\dot{m}\,C_p$	1%
G_b	4%
T_a	2°C

754 The maximum electrical output that can be extracted from the PV module is equal to
755 $P_{el}=V_{MPP}I_{MPP}$, where V_{MPP} and I_{MPP} are the voltage and current produced by the module when
756 operating at the maximum power point. During the experimental evaluation, operation under
757 maximum power output conditions was verified by adjusting the load resistance accordingly,
758 so as the product of the cell voltage times the produced current to be maximized. It must be
759 mentioned that the device employed is less accurate than a digital MPP tracker, yet much
760 more simple and inexpensive. Besides, the main objective of the present proof-of-concept
761 study is to characterize the CPVT system in terms of overall performance, which will not be
762 affected even if the PV module may not operate exactly at the point of maximum power
763 production, since the irradiation not directly converted to electricity will be instead exploited
764 as thermal power. The system electrical efficiency can be defined as:

765

766 $$\eta_{el} = \frac{V_{MPP}I_{MPP}}{A_a G_b} \tag{3}$$

767

768 where G_b is the direct irradiation and A_a is the reflector active aperture. Provided that the
769 system has reached steady-state operating conditions, the thermal efficiency can be calculated
770 as follows:

771

772 $$\eta_{th} = \frac{Q_{th}}{A_a G_b} = \frac{\dot{m}c_p\left(T_{f,out} - T_{f,in}\right)}{A_a G_b} \tag{4}$$

773

774 where $\dot{m}$, $T_{f,in}$, $T_{f,out}$ are the specified coolant mass flow rate and temperature at the receiver
775 inlet and outlet, respectively. A linear model is commonly employed for the approximation of
776 the system thermal efficiency as follows [53]:

777

778 $$\eta_{th} = \eta_0 - U_0\,\frac{\overline{T_f} - T_a}{G_b} \tag{5}$$

779

780 where η_0 is the optical efficiency, namely the efficiency achieved by the system for negligible
781 thermal losses to the environment $\overline{T_f}$ the mean coolant temperature in the receiver and U_0 is
782 the thermal-loss coefficient. The optical efficiency is correlated to the receiver intercept factor
783 and the properties of the reflector and the receiver materials as follows [37]:

784

785 $$\eta_0 = \rho\tau\alpha\gamma \tag{5}$$

786 where ρ is the total reflectance of the reflective surface, τ is the transmittance of the glass
787 cover, α the absorptance of the receiver active area and γ is the intercept factor of the
788 receiver. The system overall efficiency was calculated by the simple summation of the
789 respective thermal and electrical efficiencies, namely $\eta_{tot}=\eta_{th}+\eta_{el}$.

790   The system efficiency for the different receiver configurations considered is illustrated in a
791 comparative manner in **Figs**. **13a-c** with the water volumetric flow rate being equal to
792 30mL/s. The direct irradiation values for all the experimental points are presented in **Fig. 13d**
793 for completeness purposes. In all the cases examined, the temperature rise within the receiver
794 was in the order of 3.5-4K, depending on the operating point, while the fluid inlet temperature
795 lied in the range 298-323K. An initial observation can be made that the system optical
796 efficiency, i.e. the system overall efficiency for negligible heat losses, is in the order of 50%,
797 which implies that half of the radiation incident on the system aperture is lost due to the
798 system optical quality. Based on the results of the ray-tracing simulations for the distorted
799 parabolic shape (see **§3.2**), the intercept factor of the receiver was estimated equal to 0.57
800 (**Fig. 14**) and thus the additional 7% of irradiation lost must be attributed to the transmittance-
801 absorptance product $\tau\alpha$ of the PV module.

802   It is interesting to notice that the optical efficiency is approximately 2% higher in the
803 systems employing PV modules with 60mm-wide cells (**Figs. 13a-b**). The enhanced optical
804 efficiency is justified considering that the cell material, which has an anti-reflective coating,
805 occupies a larger module area in the case of the wide cells, while a portion of that area is
806 substituted by reflective anodized aluminum in the narrow-cell modules. The comparison of
807 **Figs. 13a-b** also reveals that the receiver employing the worse performing wide-cell module
808 (**Fig.13b**) achieves higher thermal performance compared to the receiver corresponding to
809 **Fig. 13a** due to the additional power available to be extracted as heat. Hence, the
810 interdependent nature of the electrical and thermal efficiencies of a CPVT system becomes
811 evident. In any case, the system overall efficiency is dependent only on its quality
812 characteristics, such as optical efficiency, thermal losses and possible parasitic power.

813   The maximum electrical efficiency is in the order of 7.0% and is achieved by a wide-cell
814 module (**Fig. 13a**). On the other hand, the maximum efficiency achieved by the narrow-cell
815 modules is lower and approximately equal to 5.0% (**Fig. 13c**). The discrepancy in the
816 efficiency of the two module designs is primarily attributed to the extent of their active area,
817 as the width of the solar band is even larger than the 60mm-wide cells and thus the irradiation
818 spillage outside the cell active area becomes significant especially for the narrow, 40mm-wide
819 cells (**see Fig. 7b**). Besides, the significant irradiation non-uniformity is the reason for the low
820 efficiency of all the PV modules as, besides the significant irradiation spillage, the cells are
821 primarily illuminated in the regions close to the busbar, while the bulk material at cell mid-
822 width receives irradiation of much lower intensity (see **Fig. 8**). It has been demonstrated by
823 Coventry **[15]**, that partial illumination of a solar-cell leads to significant decrease of its
824 efficiency and consequently a uniform irradiation profile across the cell width would be ideal,
825 in terms of performance. It is necessary to point out, and in reference to **Fig. 13b**, that the
826 efficiency of the PV module comprising wide cells is lower by 2% absolute than the
827 respective value for the module with identical geometrical parameters referring to **Fig. 13a**.
828 The decline in the performance of the former module occurred on grounds of improper
829 connection to the electrical load, as was identified after the testing completion and not on the
830 module manufacturing quality. However, the overall system efficiency could be reliably
831 evaluated, due to the interdependent nature of the system electrical and thermal output.
832 Hence, the experimental data obtained were reckoned as valuable for the characterization of
833 the overall system performance.

834   It is also made evident by **Fig. 13** that the system thermal efficiency exhibits a weak
835 dependence on the operating temperature, i.e. heat losses are relatively insignificant. This is

due to the cooling of the PV module, the compact heat-sink configurations and the use of heavy insulation, which lead to minimal convection and radiation losses from the PV-module front glass cover, as well as, to minimal conduction losses from the receiver back surfaces, respectively. It must be noted that the receiver configuration employing the narrow-cell module and the VW cooling device (**Fig. 13c**) was insulated using expanded polystyrene (*k=0.033 W/mK*), which seems to be a more appropriate material in comparison to Armaflex that was used for the other configurations. This is made evident by the heat-loss coefficient of the specific configuration ($U_0 \approx 0.5$ W/m^{2}K), whose value is approximately half of the respective ones obtained for the other configurations. A theoretical estimation of the receiver thermal losses, which are highly dependent on the fluctuating environmental conditions, performed in **[43]** revealed that they are in the order of experimental uncertainty. Furthermore, the power consumption of the pump required to circulate the working fluid has been measured to be in the order of 0.2 and 0.04W for the FW and VW heat-sink devices respectively, due to the small overall system length **[43]**. Hence, the deduction that the incident irradiation is approximately "split" to useful power output and optical losses is verified.

A finding of significant importance that derives from the comparison of **Figs. 13a** and **13b-c** is that the system achieves similar overall performance regardless of the employed cooling system (FW or VW device). It is rational to expect that heat spreading is significant within the receiver material layers with high thermal conductivity (aluminum substrates), as the irradiation non-uniformity on the receiver surface and the non-uniform quality of the thermal bonding between the module and the heat sink should create a fully three-dimensional temperature field within each layer. Thus, it is plausible to conclude that heat losses are well designated by the average heat-sink temperature. An experimental investigation that has been conducted to determine the thermal performance of the cooling devices **[43],** which is not presented here for brevity, verified that the values of the thermal resistance based on the average wall temperature were approximately equal for the two devices, a fact that gives grounds for the respective similar thermal performance of the CPVT system variations. Therefore, the VW heat sink design appears to be a more attractive choice for incorporation in large scale systems, whose efficiency will be significantly affected by parasitic pumping power, as a much lower pressure drop penalty in comparison to the FW design is induced. Regarding the VW design, it has been verified in **[43]** that the power required for pumping the fluid through the heat sink is reduced by approximately 85% compared to the respective required by the FW configuration. In addition, the VW configuration achieves a more uniform cooling of the solar cells, which could also enhance the electrical production of large-scale systems **[31,32]**.
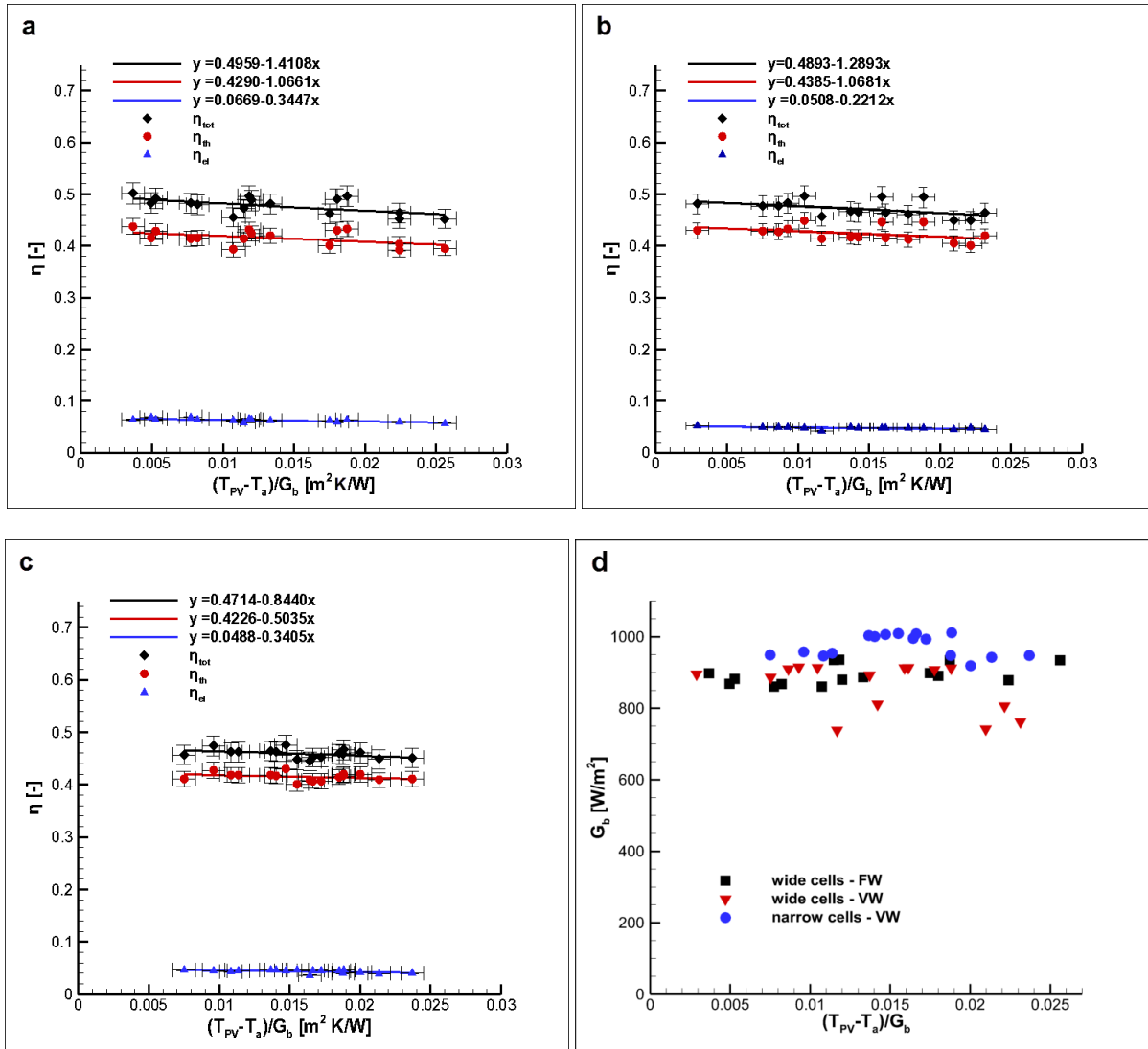
Fig. 13 Thermal (η_{th}), electrical (η_{el}) and overall (η_{tot}) efficiency of the CPVT system for flow rate 30ml/s: (a) wide cells-FW heat sink, (b) wide cells-VW heat sink, (c) narrow cells-VW heat sink.
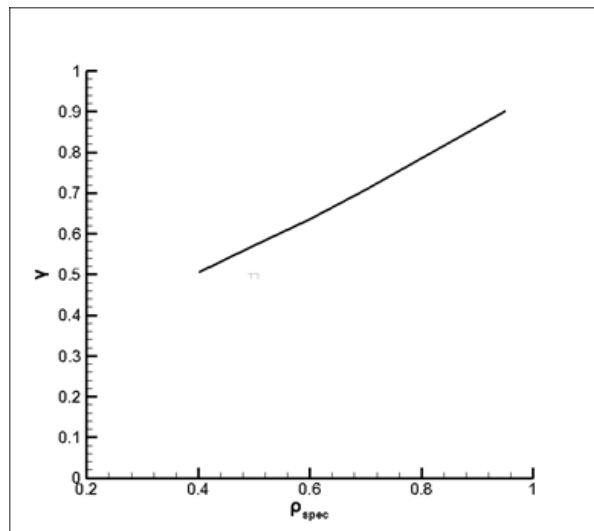

Fig. 14 Receiver intercept factor vs. specular reflectance (total reflectance equal to 95%).

5. Basic cost constituents of the CPVT system

Considering an active aperture area of 1.0 m^2 and an overall efficiency of 50% for the CPVT system, the cost per produced power, based on the actual prices of all the prototype components procured, was found to be approximately equal to 7.2 €/W. The respective cost for concentrating photovoltaic systems and concentrating solar applications, in general, is estimated to be in the range 3.0-7.5 €/W [54,55]. In any case, the newly acquired know-how in reference to the design and manufacturing of the CPVT system allows for a great margin in cost reduction, especially if a more extended production is considered.

The cost associated with the custom-made metallic parts, as reported by the industrial partners, can be reduced to 200 €/m^2 regarding the parabolic frame and to 380€ for an integrated heat sink-manifold configuration, considering a higher-volume production, e.g. of 100 items. Besides, *NAREC Ltd* estimated that for significant orders, e.g. in the range of 1000 cells, of a beforehand specified cell design, the cell cost can be reduced to as much as 15 €/cell. A PV module also comprises a low-iron glass front cover, conductive adhesive tape and an aluminum substrate. The values of low-iron glass can be as low as 35 €/m^2 for orders in the range of 50m^2. The cost for the adhesive tape could be estimated equal to 7 €/m for large orders (200 m of tape), whereas the cost for the aluminum substrate can be considered negligible. By taking into account all the cost data mentioned above the overall cost for a PV module per m^2 of CPVT system active area, provided that out-sourcing for the assembly is not required, is estimated approximately equal to 155 €.

The cost associated with the receiver insulation (Armaflex) is approximately 8 €/m^2 for orders of quantities greater than 10 m^2. The costs for all the system consituents considering the reduced values for large-scale production are shown in **Table 5**. Consequently, an estimation for the relative overall cost of a CPVT system having an active area of 1.0m^2 yields a value approximately equal to *1.75 €/W*. It must be noted that additional cost constituents, which can greatly vary depending on the system size, such as the cost of the actuator required for tracking or the inverter required in order to allow for the produced electric power to be delivered to the grid, have not been included in this analysis. In any case, it is evident that the cost per unit of produced power by the CPVT system, although it merely an initial rough estimation referring to a prototype device, is not prohibitive compared to other concentrated solar power applications.

Table 5 Cost breakdown per m^2 of active area for "large-scale" production of the CPVT system.

Component	Cost
Parabolic frame	300 €
Reflector sheets	40 €
Heat sink	180 €
Nozzles	200 €
PV modules	155 €
Insulation	0.8 €

6. Conclusions

The design, manufacturing and performance evaluation of an integrated, linear-focus CPVT system has been discussed in detail in the present study and the various technical issues associated with the realization of its sub-components have been thoroughly elucidated. A full-scale, prototype, parabolic-trough CPVT system has been successfully manufactured and experimentally investigated. The system optical analysis showed that the irradiation flux

distribution on the receiver active area was strongly affected by manufacturing limitations associated with the concentrator shape, as it was revealed that the solar beam was significantly scattered and excessive radiation spillage occurred reducing the receiver intercept factor to a value of 0.57 and the system overall optical efficiency to approximately 50%. The experimentally-obtained irradiation distribution on the receiver active area exhibited a dual peak profile, which was verified through ray-tracing simulations performed considering a parabolic trough of slightly distorted shape at its apex. The deviation of the irradiation flux profile from a normal distribution was found to have a negative effect on the electrical performance of the system, as it was confirmed through actual observation and thermal imaging that the central part of the solar cells was not properly illuminated, hindering by this way the PV module performance. The prototype CPVT system was found to achieve an overall efficiency of approximately 50% with thermal and electrical efficiencies of 43-44% and 5-7%, respectively. It was furthermore established that the PV module comprising "wide" (60.0mm) cells achieved a higher performance and was less sensitive to the increase of the operating temperature compared to that consisting of "narrow" (40.0 mm) cells. The quality of the novel heat-sink configurations developed by the authors was clearly demonstrated by the evaluation of the system thermal performance, as their incorporation in the CPVT system resulted in negligibly small thermal-losses coefficients ($U_0 \approx 0.5$-1.0 W/m^{2}K). The VW device was proved to be particularly well-suited for large scale systems, as it exhibits a similar thermal performance to the respective FW layout, however with a significantly reduced pumping-power requirement. Finally, from a techno-economical point of view, the overall cost of a commercially-produced system has been estimated at 1.75 €/W, designating the developed CPVT application a competitive option in comparison to other concentrating solar technologies.

References

[1] H.M. Henning, Solar assisted air conditioning of buildings - an overview, Appl. Therm. Eng. 27 (2007) 1734–1749.

[2] G. Mittelman, A. Kribus, A. Dayan, Solar cooling with concentrating photovoltaic/thermal (CPVT) systems, Energy Convers. Manag. 48 (2007) 2481–2490.

[3] J. Koschikowski, M. Wieghaus, M. Rommel, V.S. Ortin, B.P. Suarez, J.R. Betancort Rodríguez, Experimental investigations on solar driven stand-alone membrane distillation systems for remote areas, Desalination. 248 (2009) 125–131.

[4] H. Chang, G.B. Wang, Y.H. Chen, C.C. Li, C.L. Chang, Modeling and optimization of a solar driven membrane distillation desalination system, Renew. Energy. 35 (2010) 2714–2722.

[5] D. Du, J. Darkwa, G. Kokogiannakis, Thermal management systems for Photovoltaics (PV) installations: A critical review, Sol. Energy. 97 (2013) 238–254.

[6] A. Royne, C.J. Dey, D.R. Mills, Cooling of photovoltaic cells under concentrated illumination: A critical review, Sol. Energy Mater. Sol. Cells. 86 (2005) 451–483.

[7] L. Micheli, N. Sarmah, X. Luo, K.S. Reddy, T.K. Mallick, Opportunities and challenges in micro- and nano-technologies for concentrating photovoltaic cooling: A review, Renew. Sustain. Energy Rev. 20 (2013) 595–610.

[8] A. Royne, C.J. Dey, Design of a jet impingement cooling device for densely packed PV cells under high concentration, Sol. Energy. 81 (2007) 1014–1024.

973　[9] J. Barrau, J. Rosell, D. Chemisana, L. Tadrist, M. Ibañez, Effect of a hybrid jet impingement/micro-channel
974　cooling device on the performance of densely packed PV cells under high concentration, Sol. Energy. 85 (2011)
975　2655–2665.

976　[10] M. Rahimi, E. Karimi, M. Asadi, P. Valeh-e-Sheyda, Heat transfer augmentation in a hybrid microchannel
977　solar cell, Int. Commun. Heat Mass Transf. 43 (2013) 131–137.

978　[11] X. Han, Y. Wang, L. Zhu, The performance and long-term stability of silicon concentrator solar cells
979　immersed in dielectric liquids, Energy Convers. Manag. 66 (2013) 189–198.

980　[12] L. Zhu, Y. Wang, Z. Fang, Y. Sun, Q. Huang, An effective heat dissipation method for densely packed solar
981　cells under high concentrations, Sol. Energy Mater. Sol. Cells. 94 (2010) 133–140.

982　[13] F. Chenlo, M. Cid, A linear concentrator photovoltaic module: analysis of non-uniform illumination and
983　temperature effects on efficiency, Sol. Cells 20 (1987) 27–39.
984
985　[14] C. Gibart, S.E. De Propulsion, Study of and tests on a hybrid photovoltaic-thermal collector using
986　concentrated sunlight, Sol. Cells 4 (1981) 71–89.
987
988　[15] J.S. Coventry, Performance of a concentrating photovoltaic/thermal solar collector, Sol. Energy. 78 (2005)
989　211–222.
990
991　[16] M. Li, G.L. Li, X. Ji, F. Yin, L. Xu, The performance analysis of the Trough Concentrating Solar
992　Photovoltaic/Thermal system, Energy Convers. Manag. 52 (2011) 2378–2383.
993
994　[17] X. Yongfeng, L. Ming, W. Liuling, L. Wenxian, X. Ming, Z. Xinghua, et al., Performance analysis of solar
995　cell arrays in concentrating light intensity, J. Semicond. 30 (2009) 084011.
996
997　[18] J.I. Rosell, X. Vallverdú, M. a. Lechón, M. Ibáñez, Design and simulation of a low concentrating
998　photovoltaic/thermal system, Energy Convers. Manag. 46 (2005) 3034–3046.
999
1000　[19] M. Vivar, V. Everett, M. Fuentes, A. Blakers, A. Tanner, P. Le Lievre, M. Greaves, Initial field
1001　performance of a hybrid CPV-T microconcentrator system, Prog. Photovolt: Res. Appl. 21 (2013) 1659-1671.
1002
1003　[20] D. Chemisana, M. Ibáñez, J.I. Rosell, Characterization of a photovoltaic-thermal module for Fresnel linear
1004　concentrator, Energy Convers. Manag. 52 (2011) 3234–3240.
1005
1006　[21] P.J. Sonneveld, G.L. Swinkels, B. Van Tuijl, H.J.J. Janssen, J. Campen, G.P. Bot, Performance of a
1007　concentrated photovoltaic energy system with static linear Fresnel lenses, Sol. Energy. 85 (2011) 432–442.
1008
1009　[22] M. Chaabane, W. Charfi, H. Mhiri, P. Bournot, Performance evaluation of concentrating solar photovoltaic
1010　and photovoltaic/thermal systems, Sol. Energy. 98 (2013) 315–321.
1011
1012　[23] B. Du, E. Hu, M. Kolhe, Performance analysis of water cooled concentrated photovoltaic (CPV) system,
1013　Renew. Sustain. Energy Rev. 16 (2012) 6732–6736.
1014
1015　[24] A. Kribus, D. Kaftori, G. Mittelman, A. Hirshfeld, Y. Flitsanov, A. Dayan, A miniature concentrating
1016　photovoltaic and thermal system, Energy Convers. Manag. 47 (2006) 3582–3590.
1017
1018　[25] C. Kong, Z. Xu, Q. Yao, Outdoor performance of a low-concentrated photovoltaic-thermal hybrid system
1019　with crystalline silicon solar cells, Appl. Energy. 112 (2013) 618–625.

1020　[26] M. Brogren, P. Nostell, B. Karlsson, Optical efficiency of a PV thermal hybrid CPC module for high
1021　latitudes, Sol. Energy 69 (2000) 173-185.

[27] J. Nilsson, H. Håkansson, B. Karlsson, Electrical and thermal characterization of a PV-CPC hybrid, Sol. Energy. 81 (2007) 917–928.

[28] L.R. Bernardo, B. Perers, H. Håkansson, B. Karlsson, Performance evaluation of low concentrating photovoltaic/thermal systems: A case study from Sweden, Sol. Energy. 85 (2011) 1499–1510.

[29] R. Künnemeyer, T.N. Anderson, M. Duke, J.K. Carson, Performance of a V-trough photovoltaic/thermal concentrator, Sol. Energy. 101 (2014) 19–27.

[30] I.K. Karathanassis, E. Papanicolaou, V. Belessiotis, G.C. Bergeles, Design and optimization of a micro heat sink for concentrating/photovoltaic thermal (CPVT) systems, Appl. Therm. Eng. (59) (2013) 733–744.

[31] I.K. Karathanassis, E. Papanicolaou, V. Belessiotis, G.C. Bergeles, Three dimensional flow effects on forced convection heat transfer in a channel with stepwise-varying width, Int. J. Therm. Sci. (67) (2013) 177–191.

[32] I.K. Karathanassis, E. Papanicolaou, V. Belessiotis, G.C. Bergeles, Effect ofsecondary flows due to buoyancy and contraction on heat transfer in a twosection plate-fin heat sink, Int. J. Heat Mass Transfer (61) (2013) 583–897.

[33] I.K. Karathanassis, E. Papanicolaou, V. Belessiotis, G.C. Bergeles, Experimental and numerical evaluation of an elongated plate-fin heat sink with three sections of stepwise varying channel width, Int. J. Heat Mass Transfer (84) (2015) 16-34.

[34] Alanod Gmbh., Miro Reflecive Surface Technical Specification Brochure, Ennepetal, Germany. Available at: http://www.bluetec.eu/en/Reflection/Technical_Informations.

[35] NREL, Research Cell Efficiency Records, March 2014, available at http://www.nrel.gov/ncpv/.

[36] G. Zubi, J.L. Bernal-Agustín, G.V. Fracastoro, High concentration photovoltaic systems applying III-V cells, Renew. Sustain. Energy Rev. (13) (2009) 2645–2652.

[37] J.A. Duffie, W.A. Beckmann, Solar engineering of thermal processes, fourth ed., Wiley, New York, 2013.

[38] K.J. Riffelmann, A. Neumann, S. Ulmer, Performance enhancement of parabolic trough collectors by solar flux measurement in the focal region, Sol. Energy. (80) (2006) 1303–1313.

[39] E. Lüpfert, S. Ulmer, K. Pottler, K.J. Riffelmann, A. Neumann, B. Schiricke Parabolic trough optical performance analysis techniques, J. Sol. Energy Eng. (129) (2007) 147-152.

[40] E. Pihl, C. Thapper, Evaluation of the concentrating PVT systems MaReCo and Solar8, MSc Thesis, Lund University, Lund, 2006.

[41] K.K. Chong, T.K. Yew, Novel optical scanner using photodiodes array for two-dimensional measurement oflLight flux distribution, IEEE Trans. Instrum. Meas. (60) (2011) 2918–2925.

[42] VISHAY, BPW34 Datasheet, 2011, available at: http://www.vishay.com/docs/81521/bpw34.pdf.

[43] I.K. Karathanassis, Development and optimization of a concentrating photovoltaic/thermal cogeneration system. PhD Thesis, National Technical University of Athens, 2015.

[44] Lambda Research Corp., TracePro User's Manual, Release 5.0, Littleton, MA, 2009.

[45] W.B.Stine, R.W.Harrigan, Power from the sun, Wiley, New York, 1986, Chapter 8.

[46] DIN EN 60751:2009 Standard, Usage limitations and accuracies of platinum resistance thermometers in industrial applications.

1075   [47] Agilent Technologies Inc., VEE Pro User's guide, 8th ed., Lovoeland CO, 2004.
1076

1077   [48] R.J. Moffat, Describing the uncertainties in experimental results, Exp. Therm. Fluid. Sci. 1 (1988) 3-17.
1078

1079   [49] E. Skoplaki, J.A. Palyvos, On the temperature dependence of photovoltaic module electrical performance: A
1080   review of efficiency/power correlations, Sol. Energy. 83 (2009) 614–624.
1081

1082   [50] W. Xiao, W.G. Dunford, A. Capel, A novel method for photovoltaic cells, Proceedings of the 35th Annual
1083   IEEE Power Electronics Specialists Conference, Aachen, Germany, 2004.
1084

1085   [51] M. Vivar, M. Clarke, J. Pye, V. Everett, A review of standards for hybrid CPV-thermal systems, Renew.
1086   Sustain. Energy Rev. 16 (2012) 443–448.
1087

1088   [52] ASHRAE 93-2010 Standard, Methods of testing to determine the thermal performance of solar collectors.
1089

1090   [53] ASTM E905-87 Standard, Standard test method for determining thermal performance of tracking
1091   concentrating solar collectors, 2007.
1092

1093   [54] J.E. Haysom, O. Jafarieh, H. Anis, K. Hinzer, Concentrated photovoltaics system costs and learning curve
1094   analysis, AIP Conf. Proc. 239 (2013) 1556.
1095

1096   [55] U.S. Department of Energy, Sunshot Vision Study, February 2012, available at
1097   http://energy.gov/eere/sunshot/sunshot-vision-study.
1098